NANO LETTERS

pubs.acs.org/NanoLett Letter

Role of the Exciton–Polariton in a Continuous-Wave Optically Pumped $CsPbBr_3$ Perovskite Laser

Qiuyu Shang, Meili Li, Liyun Zhao, Dingwei Chen, Shuai Zhang, Shulin Chen, Peng Gao, Chao Shen, Jun Xing, Guichuan Xing, Bo Shen, Xinfeng Liu, and Qing Zhang*

Cite This: *Nano Lett.* 2020, 20, 6636–6643 Read Online

ACCESS | Metrics & More | Article Recommendations | Supporting Information

ABSTRACT: Lead halide perovskites have emerged as excellent optical gain materials for solution-processable and flexible lasers. Recently, continuous-wave (CW) optically driven lasing was established in perovskite crystals; however, the mechanism of low-threshold operation is still disputed. In this study, CW-pumped lasing from one-dimensional $CsPbBr_3$ nanoribbons (NBs) with a threshold of ~130 W cm^{-2} is demonstrated, which can be ascribed to the large refractive index induced by the exciton–polariton (EP) effect. Increasing the temperature reduces the exciton fraction of EPs, which decreases the group and phase refractive indices and inhibits lasing above 100 K. Thermal management, including reducing the NB height to ~120 ± 60 nm and adopting a high-thermal-conductivity sink, e.g., sapphire, is critical for CW-driven lasing, even at cryogenic temperatures. These results reveal the nature of ultralow-threshold lasing with $CsPbBr_3$ and provide insights into the construction of room-temperature CW and electrically driven perovskite macro/microlasers.

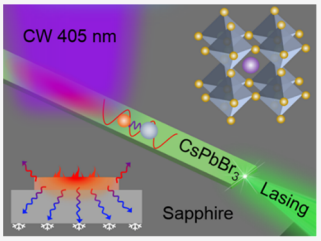

KEYWORDS: *perovskite, $CsPbBr_3$, continuous-wave laser, exciton–polariton, microlaser, low threshold*

Developing solution-processable and good-flexibility semiconductor lasers driven by continuous-wave (CW) optical and electrical injection is a long-standing challenge in optoelectronics.[1−3] Lead halide perovskites combine the advantages of organic and inorganic semiconductors and exhibit superior optical absorption, low-lying defect states, low triple accumulation, and easily engineered electronic band gaps.[4−7] Owing to these advantages, perovskites have not only attracted enormous attention for applications in solar cells, light-emitting diodes (LEDs), and photon/X-ray detectors[4−9] but also have emerged as new hybrid gain materials that can be applied to low-threshold solution-processable lasers.[10−13] Furthermore, the long-distance bipolar carrier diffusion capability greatly increases the possibility of realizing electrically pumped lasing devices.[14,15]

After amplified spontaneous emission (ASE) driven by femtosecond-pulsed lasers is demonstrated in three-dimensional perovskites, only 3 years are needed to achieve CW optically pumped lasing with perovskites.[3,16−18] This is a milestone toward realizing electrically pumped lasers. Further, solution-processed polycrystalline thin films are coupled to external high-quality distributed feedback cavities to construct vertical/side cavity surface-emitting lasers.[3] In these works, along with the high-quality cavities, the optical gain is extensively improved by the local introduction of a guest–host energy system near the phase-transition temperature of 120–160 K. This feature reduces the laser threshold to 17 kW cm^{-2}, which is the typical power density for CW operation.[3] Meanwhile, low-dimensional perovskites (i.e., monocrystalline nanowires) functioning as both gain media and optical microcavities have been studied for microlaser construction.[4,10,11,17,18] Remarkably, CW-pumped green-color lasing has been observed in $CsPbBr_3$ nanowires with a threshold of 6 kW cm^{-2}, which is comparable to that of thin films despite the limited gain volume and lower quality of the self-confined cavity.[18] The ultralow-threshold operation is preliminarily attributed to the presence of exciton–polaritons (EPs) generated by strong exciton–photon coupling, which can be extended to numerous perovskites with high exciton binding energies. However, the central issue, the role of EPs in low-threshold operation, remains to be clarified.[18−25] Additionally, improving the crystalline quality and increasing the lifetime of the metastable electronic state to ~100 ns could raise the operating temperatures of CW lasers in phase-stable polycrystalline thin films, although it is still below 120 K.[16] To realize commercial laser devices, the feasibility and challenges of room-temperature CW lasing also need to be addressed.[3,16−18,26−30]

In this study, we explore the mechanism and uncover the role of EPs for the low-threshold operation of CW-pumped $CsPbBr_3$ nanoribbon (NB) lasers. We find that EPs generate a high group refractive index (n_g ~ 60) and superior phase refractive index (n_p ~ 2.8) near the exciton resonance, which

Received: June 13, 2020
Revised: August 2, 2020
Published: August 3, 2020

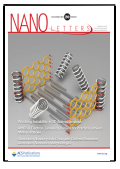

https://dx.doi.org/10.1021/acs.nanolett.0c02462
Nano Lett. 2020, 20, 6636–6643

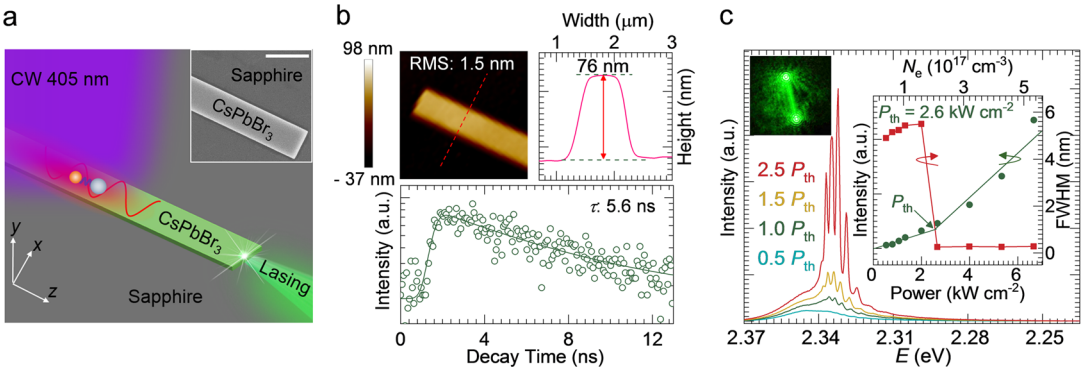

Figure 1. CW lasing characteristics of an as-grown $CsPbBr_3$ NB on the sapphire substrate at 78 K. (a) Schematic of CW lasing (405 nm excitation) of a $CsPbBr_3$ NB on the sapphire substrate. The photoexcited exciton interacts with the photon to form an EP and further propagates along the $CsPbBr_3$ NB. Inset: top view of the scanning electron microscopy image of an as-grown $CsPbBr_3$ NB. Scale bar: 2.5 μm. (b) Upper panel: atomic force microscopy image of a representative $CsPbBr_3$ NB with H = 76 nm and W = 1.2 μm. Lower panel: time-resolved photoluminescence (TRPL) spectrum of a representative $CsPbBr_3$ NB with a single-exponential lifetime of 5.6 ns. (c) CW lasing emission in a $CsPbBr_3$ NB at 78 K. The four spectra for various laser pump densities exemplify the transition from spontaneous emission ($0.5P_{th}$) via ASE (P_{th}) to lasing ($1.5P_{th}$ and $2.5P_{th}$). P_{th} = 2.6 kW cm^{-2}. Left inset: lasing image with two bright spots from the end facet with 400 nm pulsed laser excitation, indicating low far-field scattering and radiation loss. Right inset: linear scale integrated intensity (green dots) and fwhm (red dots) versus power density (excitation density) at 78 K. The corresponding excitation density at threshold is ~2.1 × 10^{17} cm^{-3}.

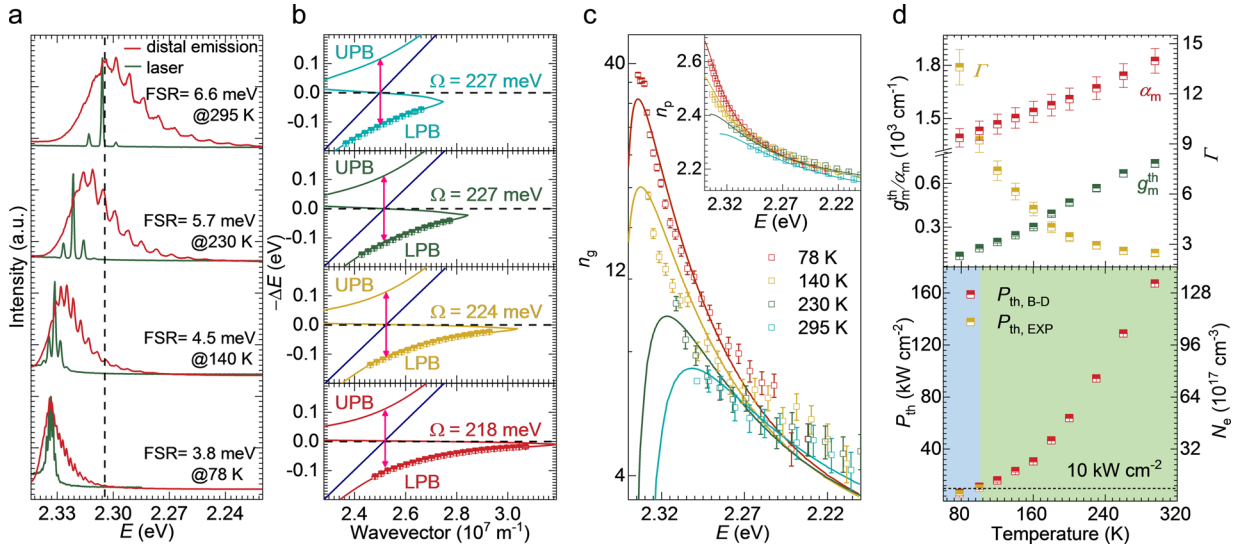

Figure 2. Temperature-dependent phase refractive index $n_p(E)$ and group refractive index $n_g(E)$ of light in an as-grown $CsPbBr_3$ NB. (a) Distal PL (red curves) spectra with 405 nm CW laser excitation and in situ lasing (green curves) spectra with pulsed laser excitation for a representative $CsPbBr_3$ NB ($L \times W \times H$ = 12.8 μm × 3.8 μm × 0.16 μm) at temperatures of 295, 230, 140, and 78 K. The FSR in the distal PL spectra decreases from 6.6 meV to 5.7, 4.5, and 3.8 meV at 2.305 eV as the temperature decreases from 295 K to 230, 140, and 78 K, respectively. (b) Fitted $E-k$ dispersions extracted from distal PL spectra in panel a with a classical Lorentz oscillator model. E_T is 2.356, 2.357, 2.357, and 2.352 eV at temperatures of 295, 230, 140, and 78 K, respectively. The corresponding values for Ω are 227, 227, 224, and 218 meV, respectively. (c) $n_g(E)$ and $n_p(E)$ (inset) calculated from the $E-k$ dispersions according to $n_g = \left(\frac{dE}{dk}\right)_{vacuum} / \left(\frac{dE}{dk}\right)_{cavity}$ and $n_p = \hbar ck/E$ at temperatures of 295, 230, 140, and 78 K. These quantities rapidly increase near E_T. (d) Upper panel: temperature-dependent modal loss α_m (red dots), required material gain threshold g_m^{th} (green dots), and Γ (yellow dots) for NB in panel a. Lower panel: (red dots) simulated temperature-dependent power density (excitation density) based on gain−loss analysis in the upper panel; (yellow dots) experimental data from CW laser measurements. Black line: P = 10 kW cm^{-2}.

increases the modal confinement by a factor of 7.7 and reduces the cavity-edge transmission loss by 19%. These improvements lead to ultralow thresholds of ~2.6 and 0.13 kW cm^{-2} at 78 and 7.8 K, respectively. We also demonstrate that increasing the temperature T significantly decreases the exciton fraction of EPs, which causes high temperature-sensitive thresholds and inhibits lasing under CW excitation above 100 K. Furthermore, heat management (i.e., thin and planar $CsPbBr_3$ NBs, as well as a substrate with high thermal conductivity and low reflectivity) is crucial even at the temperature of liquid nitrogen. These findings provide insights into the EP effect of perovskite and the development of room-temperature CW/electrically driven lasers.

Figure 1a schematically illustrates the device construction, consisting of a rectangular $CsPbBr_3$ NB on a sapphire substrate. $CsPbBr_3$ is selected as a case study, owing to its relatively good environmental and thermal stability among perovskites.[31] A sapphire substrate (thermal conductivity: 42

https://dx.doi.org/10.1021/acs.nanolett.0c02462
Nano Lett. 2020, 20, 6636−6643

W m^{-1} K^{-1}) is adopted as a superior thermal conductor to compensate for the poor thermal conductivity of $CsPbBr_3$ (0.4 W m^{-1} K^{-1});[18] the relatively low refractive index of sapphire (n_r = 1.77) ensures the well-confined photonic mode within $CsPbBr_3$ NB (n_r = 2.3). Monocrystalline orthorhombic-phase $CsPbBr_3$ NBs are fabricated using an optimized antisolvent method (Supporting Information, Note S1 and Figure S1). The NB exhibits a root-mean-square roughness of ∼1.5 nm (Figure 1b, upper panel), and the PL decays single-exponentially with a time constant of ∼5.6 ns (Figure 1b, lower panel); these are indicative of good crystal quality. In particular, most of $CsPbBr_3$ NBs exhibit planar cross sections with a height H of ∼120 ± 60 nm and width W of several microns. The large contact area and small height of the NBs ensure relatively highly efficient thermal diffusion at the $CsPbBr_3$−sapphire interface. When illuminated nonresonantly via a 405 nm CW laser at 78 K, an individual $CsPbBr_3$ NB gradually lases with a threshold P_{th} of 2.6 kW cm^{-2}. Here, the power density P is equal to the optical pumped excitation density (N_e) based on 1.0 kW cm^{-2} = 0.8 × 10^{17} cm^{-3} (Note S2). As the power density increases from 0.5 to 6.6 kW cm^{-2} (Figure 1c), the PL undergoes a transition from spontaneous emission (SE, 0.5 P_{th}) via ASE (P_{th}) to lasing (1.5 and 2.5 P_{th}). A group of narrow peaks with a full width at half-maximum (fwhm) of ∼0.3 nm arise below the electronic bandgap as P surpasses the threshold (Figure 1c, right inset). The transitions of the power dependence profile and fwhm at the threshold suggest the occurrence of lasing (Figure S2).[32,33] In addition, the PL image of a typical NB recorded by a high-resolution optical image system with a pulsed laser as the excitation source shows a clear interference pattern, supporting the feasibility of lasing and low scattering/radiation loss (Figure 1c, left inset and Figure S3). The free spectral range (FSR) between adjacent peaks $\Delta\lambda$ is inversely linear to the length L of the NB, and the lasing is mainly coupled out from the side facets of the NB, suggesting that these oscillation peaks are attributed to the resonance modes of the longitudinal Fabry−Pérot (F−P) cavity between two side facets (Figure 1c and Figure S4). The excitation density threshold (∼2.1 × 10^{17} cm^{-3}) is below the Mott density of $CsPbBr_3$ (4.7 × 10^{17}−1.0 × 10^{19} cm^{-3}), suggesting that the lasing is associated with excitons rather than the electron−hole plasma.[34−36] Furthermore, the FSR decreases from 5.5 to 2.1 meV as E increases from 2.325 to 2.337 eV, which suggests that the group refractive index n_g increases from 16.7 to 43.7. The spatial dispersion is much stronger than that described by the Sellmeier's equation and that induced by the nondegenerate electron−hole plasma;[34,37] this difference is attributable to the occurrence of a strong exciton−photon interaction.

Distal PL spectra are analyzed to probe the energy (E)−wavevector (k) dispersion in a representative $CsPbBr_3$ NB (Figure 2a, temperatures from top to bottom panels: 295, 230, 140, and 78 K) by home-built spatially resolved micro-photoluminescence (μ-PL) spectroscopy; this has been widely utilized to explore the propagating behaviors of EPs in 1D semiconductors.[18,38,39] At all temperatures, the FSR of the F−P resonant photonic modes resolved on the low-energy side of the PL spectrum decreases near the exciton resonance energy E_T. The center energies of these resonant modes are extracted and further plotted versus the wavevector (dots in Figure 2b; Note S3), which can be clearly expressed by an EP model based on the classic two-oscillator interacting theory (curves in Figure 2b).[38−41] Under nonresonant excitation, the polaritons of the upper polariton branch (UPB) are damped into the lower polariton branch (LPB) after propagating over tens of microns. Therefore, the as-detected polaritons are mainly from the LPB, which has been widely reported in previous literature.[21,31,38,42] Nevertheless, the UPB could be resolved in some NBs at cryogenic temperatures, exhibiting an anticrossing feature between UPB and LPB.[31] The Rabi splitting energy Ω measured from the maximal energy difference between the LPB and UPB (e.g., ∼227 meV under 295 K) is greater than the dissipative energy of both photons (∼15 meV) and excitons (∼67 meV), which satisfies the strong coupling condition.[38] The as-extracted n_g of the LPB polariton increases significantly near the exciton energy (e.g., from 3.2 for 2.16 eV to 6.8 for 2.29 eV at 295 K (dots in Figure 2c)). Additionally, this energy dependence of n_g is well fitted by the EP model (lines in Figure 2c), which confirms the occurrence of EPs.[43,44] The exciton fraction (effective mass) of EPs in the LPB is calculated to increase from 0.19 (0.11 × 10^{-5} m_e) to 0.68 (0.27 × 10^{-5} m_e) (Figure S5); this tendency agrees with the dispersion curves, which shows the group index increasing near the exciton resonance. Reducing the temperature enhances the spatial dispersion of EPs, which increases the group and phase refractive indices. For example, as T decreases from 295 to 78 K, the FSR of the mode at ∼2.305 eV decreases from 6.6 to 3.8 meV (black dashed line, Figure 2a). This change suggests that n_g increases from 7.2 to 12.8, while n_p increases from 2.3 to 2.35 (Figure 2c), as demonstrated by the E−k dispersion of the EPs (Figure 2b). As the temperature decreases, Ω slightly decreases from 227 to 218 meV. Moreover, the as-detected EPs in the LPB move closer to the excitonic reservoir because of the reduced phonon scattering during the propagation process under nonresonant conditions.[18] This characteristic results in a higher exciton fraction, a smaller group velocity, and higher refractive indices nearby. Finally, the group and phase refractive indices near the exciton energy, where lasing probably occurs, reach 37.5 and 2.6, respectively, at 78 K (red dots, Figure 2c).

The increases in the refractive indices lead to the reduction of the lasing threshold. In this study, a model similar to that of a surface plasmon polariton laser is considered to express the lasing of one-dimensional NB microcavities. In this model, the stimulated emission is established via population inversion of the electrons and holes, the emitted photons propagate as EPs, and the presence of EPs modifies the velocity and refractive behavior of the propagating photons inside the NB.[31,43−46] Lasing occurs when the modal optical gain Γg_m^{th} over-compensates for the modal optical loss α_m (i.e., $\Gamma g_m^{th} > \alpha_m$, with g_m^{th} and Γ being the material gain threshold and photonic confinement factor, respectively).[47,48] Increasing the group and phase refractive indices increases Γ based on the relation $\Gamma \propto n_g$ and reduces the transmission loss, respectively. The upper panel in Figure 2d shows that the absorption loss and transmission loss at the end facets decrease from 363 to 123 cm^{-1} and 1462 to 1268 cm^{-1}, respectively, as T decreases from 295 to 78 K. More importantly, the confinement factor increases from 2.5 to 13.6 (5.4 times), which reduces g_m^{th} from 737 to 102 cm^{-1}. The absorption loss decreases with temperature, owing to the suppressed phonon scattering, but the contribution to the total optical loss is significantly lower than that of the transmission loss (Notes S4 and S5).[49] The power (excitation) density threshold is further extracted under the Bernard−Duraffourg condition (Note S5 and Figure S5), which requires the differential between the quasi-Fermi levels

https://dx.doi.org/10.1021/acs.nanolett.0c02462
Nano Lett. 2020, 20, 6636−6643

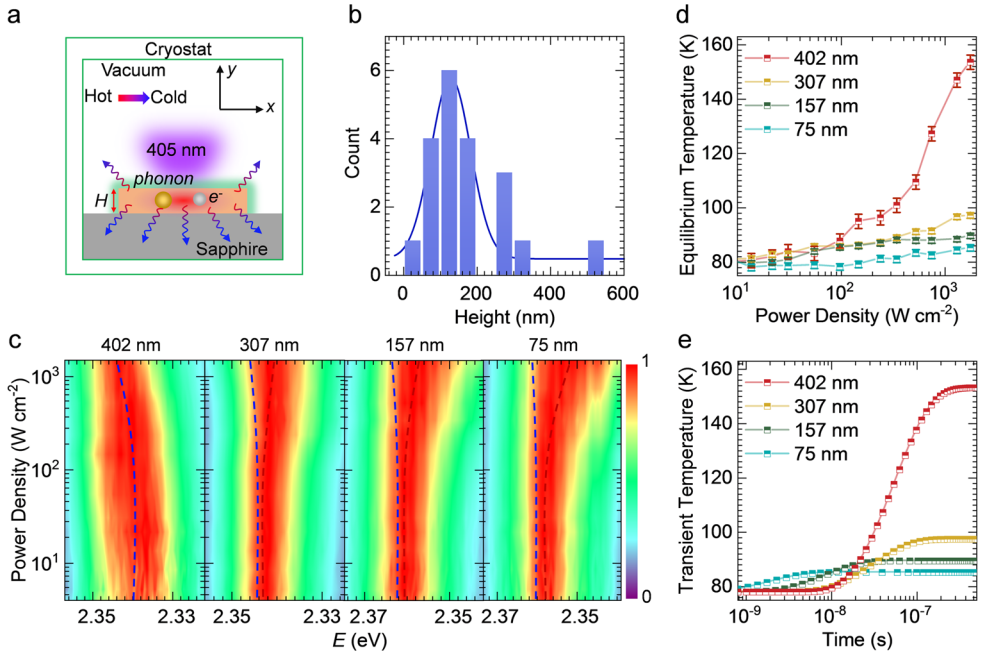

Figure 3. Height-dependent thermal diffusion in the $CsPbBr_3$ NB−sapphire structure. (a) x−y plane schematic of thermal diffusion for the NB−sapphire structure in a vacuum cryostat. The localized heat mainly diffuses by thermal radiation (vacuum, inefficient) and thermal conduction ($CsPbBr_3$ NB and sapphire, efficient). H: height of the NB. e^-: electron. (b) Statistics for the heights of as-grown $CsPbBr_3$ NBs, showing that CW lasing mainly occurs when the height is less than 400 nm and is dominant at ∼120 nm. (c) Two-dimensional pseudocolored power density-dependent PL plot for four NBs with heights of 402, 307, 157, and 75 nm ($L \times W = 10.0 \pm 2.0\ \mu m \times 2.0 \pm 0.5\ \mu m$). The blue dashed curves show that the spontaneous emission peaks are gradually blueshifted as the power density increases. For NBs with heights of 307, 157, and 75 nm, the red dashed curves show that multiple oscillating peaks (ASE) tend to emerge at high power densities. (d) Corresponding equilibrium temperature versus power density for NBs in panel c, as calculated using the thermal coefficients. (e) Simulated transient temperature versus time with P = 1.75 kW cm^{-2} at a position of $H/2$ in the NBs, as obtained using DEVICE (Lumerical Inc.).

for the electron and hole to exceed the photon energy.[16,49] The lower panel in Figure 2d shows that the estimated power density thresholds are 6.4 and 11.1 kW cm^{-2} at 78 and 100 K (red dots), respectively, which agrees with the experimental results (5.5 and 10.2 kW cm^{-2}, respectively; yellow dots). This agreement confirms the reliability of the EP model, which indicates that the reduced threshold is mainly due to the enhanced refractive indices. As T increases further, P_{th} grows rapidly, exceeding ∼10 kW cm^{-2} at 100 K (the typical threshold for CW operation; dashed line) and reaching ∼167 kW cm^{-2} at 295 K. This change suggests that CW lasing may not be sustained above ∼100 K (green area) and that cryogenic operation remains necessary. Further, the calculated operation temperature of the CW lasing and temperature-dependent threshold are in agreement with the experimental results, suggesting the reliability of the proposed lasing mechanism.

Considering the ultralow thermal conductivity of perovskite, the continuous irradiation of an excitation laser can generate a massive amount of localized heat inside an NB. This heat can locally increase the temperature and consequently reduce the refractive index, also accelerating the crystal degradation and increasing P_{th}. Therefore, controlling thermal diffusion is crucial to sustaining CW-driven lasing.[50] Most of the photon-generated heat is diffused by conduction toward the sapphire substrate via electrons and phonons (Figure 3a). Hence, thinner and planar NBs on a substrate with superior thermal conductivity are preferred. In this study, despite the variation of lasing thresholds with the width, length, and crystal quality of NBs (Figure 3b and Figure S6), CW operation is mainly achieved in NBs with $H \sim 120 \pm 60$ nm. Slightly increasing the thickness of the NBs (>300 nm) may still support CW excitation lasing, but the aspect ratio W/H should be greater than 10 to ensure efficient heat transport (Figure S6). When H < 50 nm, the photonic mode is prohibited by the optical diffraction limit, which is not the focus of this work.

The height-dependent lasing behavior is also supported by the subsequent PL spectroscopy and thermal dynamic analysis results (Figure 3c−e). Four NBs with H = 402, 307, 157, and 75 nm are selected as case studies. As P increases from 5.2 × 10^{-3} to 1.75 kW cm^{-2} (close to P_{th} at 78 K), the SE peaks of the NBs at H = 75 and 157 nm exhibit slight blue shifts (blue lines; Figure 3c and Figures S7−9), suggesting small temperature increases ΔT of 7.3 and 11.7 K, respectively (blue and green dots, Figure 3d). In contrast, the SE peaks of the NBs at H = 307 and 402 nm become progressively blueshifted by 3.3 and 5.1 meV, respectively, which suggests ΔT of ∼19.2 (yellow dots) and 75.6 K (red dots, Figure 3d), respectively. Remarkably, the stimulated emission feature could be resolved on the low-energy side of the PL spectra for the NBs at H = 75 and 157 nm as $P > 2.0 \times 10^{-1}$ kW cm^{-2} (red lines). The thermal dynamics of the NB with a different height is further analyzed (Figure 3e). For simplicity, the temperature probe is located at $H/2$ of the NBs (Figure S10), and the heat source is settled at time zero (t = 0 s, time revolution: 10^{-10} s). The transient temperatures for the NBs with H = 75 and 157 nm increase rapidly within 7 × 10^{-9} and 3 × 10^{-8} s and gradually become saturated at 85.2 and 89.5 K, respectively. Meanwhile, the transient temperatures for the NBs with H = 307 and 402 nm increase for 10^{-7} and 3 × 10^{-7} s, respectively, and reach equilibrium at 97.4 and 153.2 K, respectively. The low equilibrium temperature and short equilibrium time

https://dx.doi.org/10.1021/acs.nanolett.0c02462
Nano Lett. 2020, 20, 6636−6643

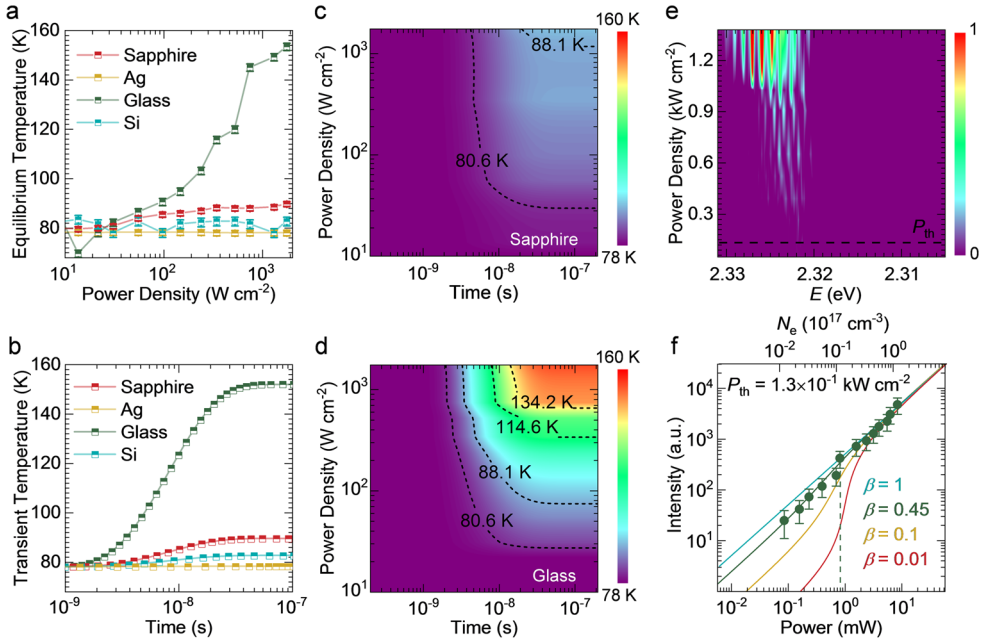

Figure 4. Thermal diffusion in $CsPbBr_3$ NBs on selected substrates at 78 K and CW lasing characteristics of as-grown $CsPbBr_3$ NB on the sapphire substrate at 7.8 K. (a) Calculated equilibrium temperature versus power density based on thermal coefficients for four NBs with $H \approx 160 \pm 20$ nm on sapphire, silver, glass, and silicon substrates ($L \times W = 10.0 \pm 2.0\ \mu m \times 2.0 \pm 0.5\ \mu m$). (b) Simulated transient temperature versus time with $P = 1.75$ kW cm^{-2} at $H/2$ in the NBs as simulated using DEVICE (Lumerical Inc.). Simulated 2D pseudocolored time−power density−transient temperature (x−y−z) plots at $H/2$ in the NBs on the (c) sapphire substrate and (d) glass substrate as simulated using DEVICE (Lumerical Inc.). Black dashed lines: transient temperatures of 80.6, 88.1, 114.6, and 134.2 K, from left to right. (e) Two-dimensional pseudocolored PL emission in a $CsPbBr_3$ NB with $L \times W \times H = 9.6\ \mu m \times 2.5\ \mu m \times 0.18\ \mu m$ under 405 nm CW laser excitation at 7.8 K. Black dashed line: $P_{th} = 0.13$ kW cm^{-2}. (f) Log−log scale integrated intensity versus power density at 7.8 K with fitted β factors of 1, 0.45, 0.1, and 0.01, respectively.

demonstrate that the thermal diffusion is more efficient in thinner NBs. The structural degradation is also accelerated at higher temperatures, and the power density-dependent TRPL spectroscopy results show that an additional nonradiative recombination process arises in the NB with H = 402 nm (Figure S11). The lower photostability of the thicker NB (Figure S11) further increases P_{th}. The simulated P_{th} for the NB with H = 402 nm is at least ∼30 kW cm^{-2} (Figure 2d), which is greater than the excitation power (1.75 kW cm^{-2}) and typical CW-driven lasing threshold (2−6 kW cm^{-2}) at 78 K.

Four substrates are selected to explore the substrate dependence of CW lasing: glass (1.4 W m^{-1} K^{-1}), sapphire, silver (429 W m^{-1} K^{-1}), and silicon (148 W m^{-1} K^{-1}).[50] Figure 4a shows that increasing P from 0.01 to 1.75 kW cm^{-2} causes ΔT of the NBs with thicknesses of ∼160 nm to increase gradually by 1.0, 4.7, and 11.7 K on Ag (yellow dots), Si (blue dots), and sapphire (red dots) substrates, respectively. However, it reaches 75.4 K for the glass substrate (green dots). The corresponding equilibrium temperatures are 79, 82.7, 89.7, and 153.4 K, respectively. According to thermal dynamics analysis of NBs with H = 160 nm, the transient temperatures at 1.75 kW cm^{-2} on Ag, Si, and sapphire increase rapidly within 3×10^{-8} s and become saturated at 78.2 (yellow dots), 82.6 (blue dots), and 89.5 K (red dots), respectively (Figure 4b). In comparison, the transient temperature for the NB on glass increases for 7×10^{-8} s and becomes saturated at 151.9 K (green dots). This corresponds to an estimated threshold of ∼30 kW cm^{-2}, which is higher than the excitation power density and prohibits the CW lasing. Despite the good conductivity of Ag and Si, the high dielectric functions of these substrates cause high radiation loss at the cavity edge, prohibiting the CW lasing (Figure S12). Figure 4c,d displays the power-dependent dynamics of the transient temperature for NBs on sapphire and glass substrates, respectively. The transient temperature is higher on the glass substrate than on the sapphire substrate at an arbitrary time. The equilibrium temperature of the NBs on sapphire slightly increases from 79.5 to 89.5 K; on glass, it greatly increases from 82.1 to 151.9 K with P = 0.01−1.75 kW cm^{-2}, resulting in a heat island. These results confirm the importance of a substrate with high thermal conductivity for CW-operation lasing.

Further, we evaluate the feasibility of electrically driven lasing based on $CsPbBr_3$ NBs. The lowest threshold achieved in this study is 2.6 kW cm^{-2} at 78 K, which is 0.4 times that previously reported to have been obtained at the same operating temperature and the lowest value among perovskite green color microlasers (Table S1). This P_{th} corresponds to a current density of ∼5.6 kA cm^{-2} and an electrically injected carrier density of 1.4×10^{19} cm^{-3} considering an external quantum efficiency of 0.1% and PL quantum yield of 70% (Note S2) under electrical operation.[51] This value is 10 times the efficient working current of perovskite-based LEDs (<0.4 kA cm^{-2}) and the onset of Auger recombination (∼10^{18} cm^{-3}) in 3D perovskite,[51,52] indicating that electrically driven lasing is not feasible at 78 K. Further, we conduct the CW lasing measurements for 17 NBs at 7.8 K (Figure S13); the threshold decreases to 0.13−1.14 kW cm^{-2}, and the lowest value occurs for an NB with H = 180 nm. Figure 4e shows the emission behavior of the NB laser at 7.8 K. It indicates that lasing occurs above P_{th} = 0.13 kW cm^{-2} (excitation power: ∼0.77 mW) and full lasing status at P = 1.4 kW cm^{-2}. At E = 2.326 eV, n_g is ∼60.0 and n_p is ∼2.8, resulting in $\Gamma \sim 21.6$ and $g_m^{th} \sim 76.5$ cm^{-1}. The spontaneous emission factor β, which is defined as the fraction of SE radiated into a specific optical mode, is

https://dx.doi.org/10.1021/acs.nanolett.0c02462
Nano Lett. 2020, 20, 6636−6643

determined to be ~0.45 (Figure 4f and Note S6); the fwhm of the lasing mode is as small as 0.05 nm (Figure S14). The P_{th} of 0.13 kW cm^{-2} corresponds to a current density of ~0.28 kA cm^{-2} and thus an electrically injected carrier density of 7.2 × 10^{17} cm^{-3}, which is within the efficient working current density of LEDs and less than the Auger recombination threshold and suggests the feasibility of electrically driven lasing. An even lower threshold is expected for NBs after further reducing the thickness without lowering the crystal/cavity quality. Additionally, a blue GaN-based LED chip can work stably with an output power of 50 mW;[53] thus, it may serve as the excitation source for demonstrated architecture with P_{th} = 0.77 mW. This feature suggests that reduced-dimension perovskite can promote the implementation of miniaturized and integrated on-chip circuits. Although EPs considerably reduce the thresholds of NB lasers, it is not evident that the demonstrated laser is a polariton laser accomplished via Bose−Einstein condensation (BEC) as has been well-explored in two-dimensional semiconductor microcavities.[54,55] This is because the evidence of a polariton laser in one-dimensional semiconductor nanowire-like microcavities has not been explored thoroughly (Note S7 and Figure S15).

In conclusion, a CW-pumped perovskite microlaser with a threshold as low as 0.13 kW cm^{-2} is successfully demonstrated for the $CsPbBr_3$ NB−sapphire geometry. The strong exciton−photon interaction enhances the refractive index, resulting in a higher modal confinement factor and lower loss and thereby reducing the lasing threshold. However, the effect is considerably suppressed as the temperature increases, owing to the decrease of exciton fractions in EPs. Utilizing a substrate with high thermal conductivity and low reflectivity as well as a thin gain material is critical to decrease the photoheat effect and realize CW lasing. These findings clarify the mechanisms of low-threshold lasing and the role of EPs in CW-pumped lasers, providing insights into the construction of low-cost and flexible lasers in optoelectronics. We also believe that the demonstrated architecture can be used in future devices to accommodate higher current densities.

■ ASSOCIATED CONTENT

Supporting Information

The Supporting Information is available free of charge at https://pubs.acs.org/doi/10.1021/acs.nanolett.0c02462.

Fabrication and structural characterization of samples; optical spectroscopy; *E-k* fitting methods; microlaser rate equations; calculations of material gain, modal loss, and threshold gain; temperature- and power density-dependent PL spectra; DEVICE simulation (PDF)

■ AUTHOR INFORMATION

Corresponding Author

Qing Zhang − *Department of Materials Science and Engineering, College of Engineering and Research Center for Wide Gap Semiconductor, Peking University, Beijing 100871, China;* orcid.org/0000-0002-6869-0381; Email: Q_zhang@pku.edu.cn

Authors

Qiuyu Shang − *Department of Materials Science and Engineering, College of Engineering, Peking University, Beijing 100871, China*

Meili Li − *Department of Materials Science and Engineering, College of Engineering, Peking University, Beijing 100871, China*

Liyun Zhao − *Department of Materials Science and Engineering, College of Engineering, Peking University, Beijing 100871, China*

Dingwei Chen − *State Key Laboratory of Superlattices and Microstructures, Institute of Semiconductors, Chinese Academy of Sciences, Beijing 100083, China*

Shuai Zhang − *CAS Key Laboratory of Standardization and Measurement for Nanotechnology, CAS Center of Excellence for Nanoscience, National Center for Nanoscience and Technology, Beijing 100190, China*

Shulin Chen − *School of Physics and Electron Microscopy Laboratory, International Center for Quantum Materials, School of Physics, Peking University, Beijing 100871, China*

Peng Gao − *School of Physics and Electron Microscopy Laboratory, International Center for Quantum Materials, School of Physics, Peking University, Beijing 100871, China;* orcid.org/0000-0003-0860-5525

Chao Shen − *State Key Laboratory of Superlattices and Microstructures, Institute of Semiconductors, Chinese Academy of Sciences, Beijing 100083, China;* orcid.org/0000-0002-3664-4874

Jun Xing − *Key Laboratory of Eco-Chemical Engineering, Ministry of Education, College of Chemistry and Molecular Engineering, Qingdao University of Science and Technology, Qingdao 266042, China*

Guichuan Xing − *Joint Key Laboratory of the Ministry of Education, Institute of Applied Physics and Materials Engineering, University of Macau, Macao 999078, China;* orcid.org/0000-0003-2769-8659

Bo Shen − *School of Physics and Research Center for Wide Gap Semiconductor, Peking University, Beijing 100871, China*

Xinfeng Liu − *CAS Key Laboratory of Standardization and Measurement for Nanotechnology, CAS Center of Excellence for Nanoscience, National Center for Nanoscience and Technology, Beijing 100190, China;* orcid.org/0000-0002-7662-7171

Complete contact information is available at: https://pubs.acs.org/10.1021/acs.nanolett.0c02462

Author Contributions

Q.Z. conceived the idea and designed the experiments. Q.Z. and Q.S. wrote the manuscript. Q.S. and M.L. prepared the samples and performed the PL spectroscopy measurements. Q.S., M.L., L.Z., D.C., S.Z., and S.C. performed SEM, TEM, and XRD. Q.Z. led the project. All of the authors wrote the manuscript.

Notes

The authors declare no competing financial interest.

■ ACKNOWLEDGMENTS

This work was supported by funding from the Natural Science Foundation of China (51991340, 51991344, 21673054, and 11874130), Ministry of Science and Technology (2017YFA0205700, 2017YFA0304600, 2016YFA0200700, and 2017YFA0205004), Strategic Priority Research Program of Chinese Academy of Sciences (XDB36000000), Opening Project of State Key Laboratory of Bioelectronics of Southeast University, and Open Research Fund Program of the State Key Laboratory of Low-dimensional Quantum Physics (KF201907). G.X. acknowledges financial support from the

https://dx.doi.org/10.1021/acs.nanolett.0c02462
Nano Lett. 2020, 20, 6636−6643

Macau Science and Technology Development Fund (FDCT-091/2017/A2), a research grant (MYRG2018-00148-IAPME) from the University of Macau, the Natural Science Foundation of China (91733302, 61605073, and 61935017), and the Natural Science Foundation of Guangdong Province, China (2019A1515012186).

REFERENCES

(1) Park, H.-G.; Kim, S.-H.; Kwon, S.-H.; Ju, Y.-G.; Yang, J.-K.; Baek, J.-H.; Kim, S.-B.; Lee, Y.-H. Electrically driven single-cell photonic crystal laser. *Science* **2004**, *305*, 1444−1447.
(2) Eaton, S. W.; Fu, A.; Wong, A. B.; Ning, C.-Z.; Yang, P. Semiconductor nanowire lasers. *Nat. Rev. Mater.* **2016**, *1*, 16028.
(3) Jia, Y.; Kerner, R. A.; Grede, A. J.; Rand, B. P.; Giebink, N. C. Continuous-wave lasing in an organic-inorganic lead halide perovskite semiconductor. *Nat. Photonics* **2017**, *11*, 784−788.
(4) Fu, Y.; Zhu, H.; Chen, J.; Hautzinger, M. P.; Zhu, X. Y.; Jin, S. Metal halide perovskite nanostructures for optoelectronic applications and the study of physical properties. *Nat. Rev. Mater.* **2019**, *4*, 169−188.
(5) Sutherland, B. R.; Sargent, E. H. Perovskite photonic sources. *Nat. Photonics* **2016**, *10*, 295−302.
(6) Stranks, S. D.; Snaith, H. J. Metal-halide perovskites for photovoltaic and light-emitting devices. *Nat. Nanotechnol.* **2015**, *10*, 391−402.
(7) Sum, T. C.; Mathews, N. Advancements in perovskite solar cells: photophysics behind the photovoltaics. *Energy Environ. Sci.* **2014**, *7*, 2518−2534.
(8) Wang, H.; Sui, N.; Bai, X.; Zhang, Y.; Rice, Q.; Seo, F. J.; Zhang, Q.; Colvin, V. L.; Yu, W. W. Emission recovery and stability enhancement of inorganic perovskite quantum dots. *J. Phys. Chem. Lett.* **2018**, *9*, 4166−4173.
(9) Lu, D.; Zhang, Y.; Lai, M.; Lee, A.; Xie, C.; Lin, J.; Lei, T.; Lin, Z.; Kley, C. S.; Huang, J.; Rabani, E.; Yang, P. Giant light-emission enhancement in lead halide perovskites by surface oxygen passivation. *Nano Lett.* **2018**, *18*, 6967−6973.
(10) Zhu, H.; Fu, Y.; Meng, F.; Wu, X.; Gong, Z.; Ding, Q.; Gustafsson, M. V.; Trinh, M. T.; Jin, S.; Zhu, X. Y. Lead halide perovskite nanowire lasers with low lasing thresholds and high quality factors. *Nat. Mater.* **2015**, *14*, 636−642.
(11) Eaton, S. W.; Lai, M.; Gibson, N. A.; Wong, A. B.; Dou, L.; Ma, J.; Wang, L.-W.; Leone, S. R.; Yang, P. Lasing in robust cesium lead halide perovskite nanowires. *Proc. Natl. Acad. Sci. U. S. A.* **2016**, *113*, 1993−1998.
(12) Wang, Y.; Li, X.; Zhao, X.; Xiao, L.; Zeng, H.; Sun, H. Nonlinear absorption and low-threshold multiphoton pumped stimulated emission from all-Inorganic perovskite nanocrystals. *Nano Lett.* **2016**, *16*, 448−453.
(13) Huang, C.; Zhang, C.; Xiao, S.; Wang, Y.; Fan, Y.; Liu, Y.; Zhang, N.; Qu, G.; Ji, H.; Han, J.; Ge, L.; Kivshar, Y.; Song, Q. Ultrafast control of vortex microlasers. *Science* **2020**, *367*, 1018−1021.
(14) Stranks, S. D.; Eperon, G. E.; Grancini, G.; Menelaou, C.; Alcocer, M. J.; Leijtens, T.; Herz, L. M.; Petrozza, A.; Snaith, H. J. Electron-hole diffusion lengths exceeding 1 micrometer in an organometal trihalide perovskite absorber. *Science* **2013**, *342*, 341−344.
(15) Xing, G.; Mathews, N.; Sun, S.; Lim, S. S.; Lam, Y. M.; Grätzel, M.; Mhaisalkar, S.; Sum, T. C. Long-range balanced electron-and hole-transport lengths in organic-inorganic $CH_3NH_3PbI_3$. *Science* **2013**, *342*, 344−347.
(16) Brenner, P.; Bar-On, O.; Jakoby, M.; Allegro, I.; Richards, B. S.; Paetzold, U. W.; Howard, I. A.; Scheuer, J.; Lemmer, U. Continuous wave amplified spontaneous emission in phase-stable lead halide perovskites. *Nat. Commun.* **2019**, *10*, 1−7.
(17) Dong, H.; Zhang, C.; Liu, X.; Yao, J.; Zhao, Y. S. Materials chemistry and engineering in metal halide perovskite lasers. *Chem. Soc. Rev.* **2020**, *49*, 951−982.
(18) Evans, T. J. S.; Schlaus, A.; Fu, Y.; Zhong, X.; Atallah, T. L.; Spencer, M. S.; Brus, L. E.; Jin, S.; Zhu, X. Y. Continuous-wave lasing in cesium lead bromide perovskite nanowires. *Adv. Opt. Mater.* **2018**, *6*, 1700982.
(19) Su, R.; Ghosh, S.; Wang, J.; Liu, S.; Diederichs, C.; Liew, T. C. H.; Xiong, Q. Observation of exciton polariton condensation in a perovskite lattice at room temperature. *Nat. Phys.* **2020**, *16*, 301−306.
(20) Fieramosca, A.; Polimeno, L.; Ardizzone, V.; De Marco, L.; Pugliese, M.; Maiorano, V.; De Giorgi, M.; Dominici, L.; Gigli, G.; Gerace, D.; Ballarini, D.; Sanvitto, D. Two-dimensional hybrid perovskites sustaining strong polariton interactions at room temperature. *Sci. Adv.* **2019**, *5*, No. eaav9967.
(21) Su, R.; Wang, J.; Zhao, J.; Xing, J.; Zhao, W.; Diederichs, C.; Liew, T. C. H.; Xiong, Q. Room temperature long-range coherent exciton polariton condensate flow in lead halide perovskites. *Sci. Adv.* **2018**, *4*, No. eaau0244.
(22) Wang, X.; Shoaib, M.; Wang, X.; Zhang, X.; He, M.; Luo, Z.; Zheng, W.; Li, H.; Yang, T.; Zhu, X.; Ma, L.; Pan, A. High-quality in-plane aligned $CsPbX_3$ perovskite nanowire lasers with composition-dependent strong exciton-photon coupling. *ACS Nano* **2018**, *12*, 6170−6178.
(23) Shang, Q.; Zhang, S.; Liu, Z.; Chen, J.; Yang, P.; Li, C.; Li, W.; Zhang, Y.; Xiong, Q.; Liu, X.; Zhang, Q. Surface plasmon enhanced strong exciton-photon Coupling in hybrid inorganic-organic perovskite nanowires. *Nano Lett.* **2018**, *18*, 3335−3343.
(24) Dang, N. H. M.; Gerace, D.; Drouard, E.; Trippé-Allard, G.; Lédée, F.; Mazurczyk, R.; Deleporte, E.; Seassal, C.; Nguyen, H. S. Tailoring dispersion of room-temperature exciton-polaritons with perovskite-based subwavelength metasurfaces. *Nano Lett.* **2020**, *20*, 2113−2119.
(25) Bouteyre, P.; Nguyen, H. S.; Lauret, J.-S.; Trippé-Allard, G.; Delport, G.; Lédée, F.; Diab, H.; Belarouci, A.; Seassal, C.; Garrot, D.; Bretenaker, F.; Deleporte, E. Room-temperature cavity polaritons with 3D hybrid perovskite: toward large-surface polaritonic devices. *ACS Photonics* **2019**, *6*, 1804−1811.
(26) Li, Z.; Moon, J.; Gharajeh, A.; Haroldson, R.; Hawkins, R.; Hu, W.; Zakhidov, A.; Gu, Q. Room-temperature continuous-wave operation of organometal halide perovskite lasers. *ACS Nano* **2018**, *12*, 10968−10976.
(27) Brenner, P.; Paetzold, U. W.; Turnbull, G. A.; Giebink, N. C.; Samuel, I. D. W.; Lemmer, U.; Howard, I. A. Comment on "Room-temperature continuous-wave operation of organometal halide perovskite lasers. *ACS Nano* **2019**, *13*, 12257−12258.
(28) Gao, Y.; Zhao, L.; Shang, Q.; Li, C.; Liu, Z.; Li, Q.; Wang, X.; Zhang, Q. Photoluminescence properties of ultrathin $CsPbCl_3$ nanowires on mica substrate. *J. Semicond.* **2019**, *40*, 052201.
(29) Li, Q.; Li, C.; Shang, Q.; Zhao, L.; Zhang, S.; Gao, Y.; Liu, X.; Wang, X.; Zhang, Q. Lasing from reduced dimensional perovskite microplatelets: Fabry-Pérot or whispering-gallery-mode? *J. Chem. Phys.* **2019**, *151*, 211101.
(30) Liu, Z.; Shang, Q.; Li, C.; Zhao, L.; Gao, Y.; Li, Q.; Chen, J.; Zhang, S.; Liu, X.; Fu, Y.; Zhang, Q. Temperature-dependent photoluminescence and lasing properties of $CsPbBr_3$ nanowires. *Appl. Phys. Lett.* **2019**, *114*, 101902.
(31) Shang, Q.; Li, C.; Zhang, S.; Liang, Y.; Liu, Z.; Liu, X.; Zhang, Q. Enhanced optical absorption and slowed light of reduced-dimensional $CsPbBr_3$ nanowire crystal by exciton-polariton. *Nano Lett.* **2020**, *20*, 1023−1032.
(32) Johnson, J. C.; Choi, H.-J.; Knutsen, K. P.; Schaller, R. D.; Yang, P.; Saykally, R. J. Single gallium nitride nanowire lasers. *Nat. Mater.* **2002**, *1*, 106−110.
(33) O'Carroll, D.; Lieberwirth, I.; Redmond, G. Microcavity effects and optically pumped lasing in single conjugated polymer nanowires. *Nat. Nanotechnol.* **2007**, *2*, 180−184.
(34) Schlaus, A. P.; Spencer, M. S.; Miyata, K.; Liu, F.; Wang, X.; Datta, I.; Lipson, M.; Pan, A.; Zhu, X. Y. How lasing happens in $CsPbBr_3$ perovskite nanowires. *Nat. Commun.* **2019**, *10*, 265.
(35) Butkus, J.; Vashishtha, P.; Chen, K.; Gallaher, J. K.; Prasad, S. K. K.; Metin, D. Z.; Laufersky, G.; Gaston, N.; Halpert, J. E.;

https://dx.doi.org/10.1021/acs.nanolett.0c02462
Nano Lett. 2020, 20, 6636−6643

Hodgkiss, J. M. The Evolution of Quantum Confinement in $CsPbBr_3$ Perovskite Nanocrystals. *Chem. Mater.* **2017**, *29*, 3644−3652.
(36) Zhang, Q.; Su, R.; Liu, X.; Xing, J.; Sum, T. C.; Xiong, Q. High-quality whispering-gallery-mode lasing from cesium lead halide perovskite nanoplatelets. *Adv. Funct. Mater.* **2016**, *26*, 6238−6245.
(37) Liu, J.; Lee, S.; Ahn, Y. H.; Park, J.-Y.; Koh, K. H.; Park, K. H. Identification of dispersion-dependent hexagonal cavity modes of an individual ZnO nanonail. *Appl. Phys. Lett.* **2008**, *92*, 263102.
(38) van Vugt, L. K.; Piccione, B.; Cho, C. H.; Nukala, P.; Agarwal, R. One-dimensional polaritons with size-tunable and enhanced coupling strengths in semiconductor nanowires. *Proc. Natl. Acad. Sci. U. S. A.* **2011**, *108*, 10050−10055.
(39) Kang, J.-W.; Song, B.; Liu, W.; Park, S.-J.; Agarwal, R.; Cho, C.-H. Room temperature polariton lasing in quantum heterostructure nanocavities. *Sci. Adv.* **2019**, *5*, No. eaau9338.
(40) Park, K.-D.; May, M. A.; Leng, H.; Wang, J.; Kropp, J. A.; Gougousi, T.; Pelton, M.; Raschke, M. B. Tip-enhanced strong coupling spectroscopy, imaging, and control of a single quantum emitter. *Sci. Adv.* **2019**, *5*, No. eaav5931.
(41) Zhang, Q.; Liu, X. Exciton-polaritons in semiconductors. *J. Semicond.* **2019**, *40*, 090401.
(42) Sun, L.; Chen, Z.; Ren, Q.; Yu, K.; Bai, L.; Zhou, W.; Xiong, H.; Zhu, Z.; Shen, X. Direct observation of whispering gallery mode polaritons and their dispersion in a ZnO tapered microcavity. *Phys. Rev. Lett.* **2008**, *100*, 156403.
(43) Takazawa, K.; Inoue, J.-i.; Mitsuishi, K.; Takamasu, T. Fraction of a millimeter propagation of exciton polaritons in photoexcited nanofibers of organic dye. *Phys. Rev. Lett.* **2010**, *105*, 067401.
(44) Zhang, C.; Zou, C.-L.; Yan, Y.; Hao, R.; Sun, F.-W.; Han, Z.-F.; Zhao, Y. S.; Yao, J. Two-photon pumped lasing in single-crystal organic nanowire exciton polariton resonators. *J. Am. Chem. Soc.* **2011**, *133*, 7276−7279.
(45) Oulton, R. F.; Sorger, V. J.; Zentgraf, T.; Ma, R.-M.; Gladden, C.; Dai, L.; Bartal, G.; Zhang, X. Plasmon lasers at deep subwavelength scale. *Nature* **2009**, *461*, 629−632.
(46) Barnes, W. L.; Dereux, A.; Ebbesen, T. W. Surface plasmon subwavelength optics. *Nature* **2003**, *424*, 824−830.
(47) Su, Y.; Chang, P.; Lin, C.; Helmy, A. S. Record Purcell factors in ultracompact hybrid plasmonic ring resonators. *Sci. Adv.* **2019**, *5*, No. eaav1790.
(48) Saleh, A. A. E.; Dionne, J. A. Waveguides with a silver lining: Low threshold gain and giant modal gain in active cylindrical and coaxial plasmonic devices. *Phys. Rev. B: Condens. Matter Mater. Phys.* **2012**, *85*, 045407.
(49) Chen, R.; Tran, T.-T. D.; Ng, K. W.; Ko, W. S.; Chuang, L. C.; Sedgwick, F. G.; Chang-Hasnain, C. Nanolasers grown on silicon. *Nat. Photonics* **2011**, *5*, 170−175.
(50) Adachi, M. M.; Fan, F.; Sellan, D. P.; Hoogland, S.; Voznyy, O.; Houtepen, A. J.; Parrish, K. D.; Kanjanaboos, P.; Malen, J. A.; Sargent, E. H. Microsecond-sustained lasing from colloidal quantum dot solids. *Nat. Commun.* **2015**, *6*, 1−8.
(51) Leyden, M. R.; Terakawa, S.; Matsushima, T.; Ruan, S.; Goushi, K.; Auffray, M.; Sandanayaka, A. S.; Qin, C.; Bencheikh, F.; Adachi, C. Distributed feedback lasers and light-emitting diodes using 1-naphthylmethylamnonium low-dimensional perovskite. *ACS Photonics* **2019**, *6*, 460−466.
(52) Wehrenfennig, C.; Eperon, G. E.; Johnston, M. B.; Snaith, H. J.; Herz, L. M. High charge carrier mobilities and lifetimes in organolead trihalide perovskites. *Adv. Mater.* **2014**, *26*, 1584−1589.
(53) Fu, X.; Zhang, B.; Kang, X.; Deng, J.; Xiong, C.; Dai, T.; Jiang, X.; Yu, T.; Chen, Z.; Zhang, G. Y. GaN-based light-emitting diodes with photonic crystals structures fabricated by porous anodic alumina template. *Opt. Express* **2011**, *19*, A1104−A1108.
(54) Deng, H.; Weihs, G.; Santori, C.; Bloch, J.; Yamamoto, Y. Condensation of semiconductor microcavity exciton polaritons. *Science* **2002**, *298*, 199−202.
(55) Kasprzak, J.; Richard, M.; Kundermann, S.; Baas, A.; Jeambrun, P.; Keeling, J. M. J.; Marchetti, F. M.; Szymańska, M. H.; André, R.; Staehli, J. L.; Savona, V.; Littlewood, P. B.; Deveaud, B.; Dang, L. S. Bose−Einstein condensation of exciton polaritons. *Nature* **2006**, *443*, 409−414.

https://dx.doi.org/10.1021/acs.nanolett.0c02462
Nano Lett. 2020, 20, 6636−6643